Chemical Engineering Science 114 (2014) 30–39

Contents lists available at ScienceDirect

Chemical Engineering Science

journal homepage: www.elsevier.com/locate/ces

Operating ranges of gas–liquid capillary microseparators: Experiments and theory

Mark D. Roydhouse [a], Marc Pradas [b], Noor Al-Rifai [a], Benjamin Azizi [a], Enhong Cao [a], Serafim Kalliadasis [b,*], Asterios Gavriilidis [a,**]

[a] Department of Chemical Engineering, University College London, London WC1E 7JE, UK
[b] Department of Chemical Engineering, Imperial College London, London SW7 2AZ, UK

HIGHLIGHTS

- We study the breakthrough pressures (operating ranges) of capillary microseparators.
- Capillaries with either constant or tapered cross-sectional area are considered.
- Gas-to-liquid breakthrough pressure is in qualitative agreement with theory.
- Liquid-to-gas breakthrough pressure depends nonlinearly on the flow rate.
- A new theoretical approach that captures such nonlinear behaviour is developed.

ARTICLE INFO

Article history:
Received 12 November 2013
Received in revised form
1 April 2014
Accepted 15 April 2014
Available online 23 April 2014

Keywords:
Microfluidic
Multiphase flow
Microstructure
Separations

ABSTRACT

An experimental and theoretical study of capillary gas/liquid phase microseparators is presented. The device studied comprises a main microchannel with a set of capillaries fabricated to each side so that the liquid (wetting) phase can be separated from the gas (non-wetting) phase due to capillary effects. Different units are employed with different characteristics of capillaries (constant or tapered cross-sectional area and capillary size). We study how complete separation depends on the externally controlled pressure difference at the liquid and the gas outlet and how separation is affected by the imposed inlet flow rate. The results demonstrate that the operability pressure window becomes narrower as the fluid flow rates increase, and reveal discrepancies with theoretical predictions based on a simple Hagen–Poiseuille formulation. This is addressed by a new equation that takes into account interface curvature effects, and is found to be in qualitative agreement with the experimental results. In addition, we perform CFD simulations observing the emergence of interface breaking at high flow rates.
© 2014 Elsevier Ltd. All rights reserved.

1. Introduction

Microchemical processing devices offer important advantages over more traditional large-scale technologies including small operating volume, ease of use, and excellent control of the fluids involved. As a result, they have seen an explosive growth over the past decade with a wide spectrum of applications found not only in engineering and technology (Hessel et al., 2005; Geschke et al., 2004) but also in biological, chemical and physical settings (see e.g. Squires and Quake, 2005; Whitesides, 2006; Sahoo et al., 2007).

For multistep chemical synthesis, where reactors are integrated with separation units, often phase separation between gas/liquid or liquid/liquid phases needs to be accomplished. Such a phase separation is typically based on surface forces and associated capillary phenomena (Krajl et al., 2007; Gaakeer et al., 2012; Bannock et al., 2013; Adamo et al., 2013; TeGrotenhuis and Stenkamp, 2001; Günther et al., 2005; Hsieh et al., 2006; Kraus and Krewer, 2011; Hartman et al., 2009; Castell et al., 2009). A typical device consists of a series of small capillaries regularly spaced which are interconnected to a main microchannel for which a gas–liquid (multiphase) flow is passing through. The capillaries can be microfabricated as part of the separator or be present in passive membranes sandwiched between inlet and outlet microchannels (TeGrotenhuis and Stenkamp, 2001; Günther et al., 2005; Hsieh et al., 2006; Kraus and Krewer, 2011). Capillary pressure is used to exclude the gas (non-wetting) phase from entering the small channels while the liquid (wetting) phase fills the capillaries. In this situation we have complete phase separation and the microdevice works efficiently. Achieving this

* Corresponding author.
** Corresponding author.
E-mail addresses: s.kalliadasis@imperial.ac.uk (S. Kalliadasis), a.gavriilidis@ucl.ac.uk (A. Gavriilidis).

http://dx.doi.org/10.1016/j.ces.2014.04.017
0009-2509/© 2014 Elsevier Ltd. All rights reserved.

requires, however, careful tuning of the control parameters of the system (Hartman et al., 2009; Castell et al., 2009). For a given inlet flow rate, for instance, one usually needs to find the operating range of the pressure difference between the gas outlet and the liquid outlet, the limits of which are determined by the gas-to-liquid breakthrough pressure difference (i.e. the critical pressure difference above which the gas phase starts to appear in the liquid outlet) and the liquid-to-gas breakthrough pressure difference (i.e. the critical pressure difference below which the liquid phase appears in the gas outlet).

Despite the use of capillary microseparators in continuous flow conditions there has not been as of yet a clear understanding of what the operating ranges are (i.e. breakthrough pressure differences), and in particular how these ranges depend on the imposed flow in the system.

In this paper, we perform a detailed experimental study to investigate how pressure operating ranges are affected by flow. A theoretical analysis for the liquid to gas breakthrough limit and exploratory CFD work are used to provide insight into the operation of such devices.

2. Background

The main feature of downsizing a separator is that as the capillary's cross-sectional area is reduced the capillary pressure increases, and the pressure drop across the channel also increases which in turn makes the separators efficient devices at the microscale. In a gas–liquid system, gas will be excluded from the capillaries as long as the pressure difference between both phases, i.e. $\Delta P = P_G - P_L$, is less than the gas-to-liquid breakthrough pressure difference ($\Delta P_{G>L}$) which theoretically is at least equal to the capillary pressure difference (Bonn et al., 2009)

$$\Delta P_c = \gamma\kappa = \gamma\left(\frac{1}{R_1}+\frac{1}{R_2}\right), \tag{1}$$

where γ is the surface tension and κ is the interface curvature which can be expressed in terms of R_1 and R_2, the principal radii of curvature of the interface. In the case of a rectangle of sides d and h the above equation reduces to (Bruus, 2008)

$$\Delta P_c = 2\gamma\ \cos\ \theta_{eq}\left(\frac{1}{d}+\frac{1}{h}\right), \tag{2}$$

with θ_{eq} being the equilibrium contact angle. Note that, for static conditions, breakthrough of gas to liquid occurs for $\cos\ \theta = 1$, i.e. when maximum curvature is achieved, while breakthrough of liquid to gas occurs for $\theta = \theta_{eq} + 90^\circ$ (Amador et al., 2003; Butt et al., 2013). Thus the criterion for gas-to-liquid breakthrough is

$$\Delta P > 2\gamma\left(\frac{1}{d}+\frac{1}{h}\right) = \Delta P_{G>L}. \tag{3}$$

On the other hand, liquid will be excluded from the gas phase (i.e. it will not be collected at the gas outlet) as long as the inlet total flow rate Q is equal to or less than the sum of the local liquid flow rates for each capillary of the microseparator. Total and not liquid flow rate is considered as a worst case scenario, since the total flow rate determines the speed of the liquid slugs. If the slugs are very long, during the time period they spend in the main channel, the capillaries will have to pull liquid at the same rate as the total flow rate in the main channel. If there are a total number of N capillaries at the sides of the main channel, the liquid-to-gas breakthrough pressure difference $\Delta P_{L>G}$ is then obtained by taking $Q = Nq$, where q is the local flow rate at each capillary which we assume to be given by the Hagen–Poiseuille law (note that we are assuming here that the pressure drop between the end of the capillaries and the measurement location is negligible as compared to that along the capillaries). In particular, for a rectangular channel, Mortensen et al. (2005) showed that the pressure drop is given as

$$\Delta P = \frac{\alpha\eta L}{A^2}q, \tag{4}$$

where η is the liquid viscosity, L and A are the length and the cross-sectional area of the capillary, respectively, and α is a geometric factor, which was approximated based on finite-element simulations of the Poisson equation as

$$\alpha \approx \frac{22}{7}C - \frac{65}{3}, \tag{5}$$

where C is the compactness factor $C = P_r^2/A$, with P_r being the perimeter (see also the work of Bahrami et al., 2007 for an alternative equation with slightly different coefficients). We obtain hence the following condition for liquid-to-gas breakthrough:

$$\Delta P < \frac{\alpha\eta L}{NA^2}Q = \Delta P_{L>G}^{HP}, \tag{6}$$

where we have used the superscript HP to refer to a Hagen–Poiseuille prescription. However, as we shall demonstrate, our experimental results exhibit a different behaviour from that obtained by the above formulation indicating that additional effects come into play.

3. Experimental setup

Fig. 1a shows a schematic representation of the apparatus used to observe capillary separation of gas and liquid, and Fig. 1b shows a picture of the device. The chip contained N capillaries located at both sides of a main microchannel of width w and height h in which liquid and gas flowed in a slug flow pattern (see Fig. 1c). The capillaries were separated by a distance r_s and the separated liquid was collected by two ducts that channelled it to a common output. The length of the capillaries in all separators was $L = 100\ \mu m$. The main channel continued past the capillaries and carried the separated gas to an output. The chip was placed in a stainless steel compression chuck. A gas tight seal was maintained by 'O' rings on either side of the chip. Tubing was connected by Upchurch 10–32 ports. The capillaries were observed via a window in the upper portion of the chuck (cf. Fig. 1b). PFA 1/16″ OD, 1 mm ID tubing with Swagelok 316 stainless steel fittings was used for all connections. The total pressure drop of the gas outlet from the capillaries to the off-chip back pressure regulator was calculated to be 4.95×10^{-3} kPa for pure gas flow. The maximum pressure drop of the liquid (water) outlet from the collection ducts to the off-chip back pressure regulator via the bottle trap was calculated to be 0.31 kPa for pure liquid flow.

Table 1 depicts the specification for the different separators used and Figs. 2 and 3 show the corresponding microscope images of the P-series and GLS separators, respectively. Separators P1, P2, and P3 have tapered capillaries with d_i being smaller than d_o, P4 has straight capillaries and GLS is designed with d_i being larger than d_o.

3.1. Microseparator fabrication

The separator chips were fabricated using conventional semiconductor processing techniques. The silicon wafers were rinsed with de-ionised water and dried at 150–200 °C for 10 min. A thick photoresist layer (Rohm and Haas, SPR-220-7) was spin-coated on a wafer at 4000 rpm, followed by soft-baking at 110 °C for 90 min. The separator patterns from a photomask were transferred to the photoresist layer using a contact aligner (Quintel Q4000-6). The exposure energy for the photoresist was

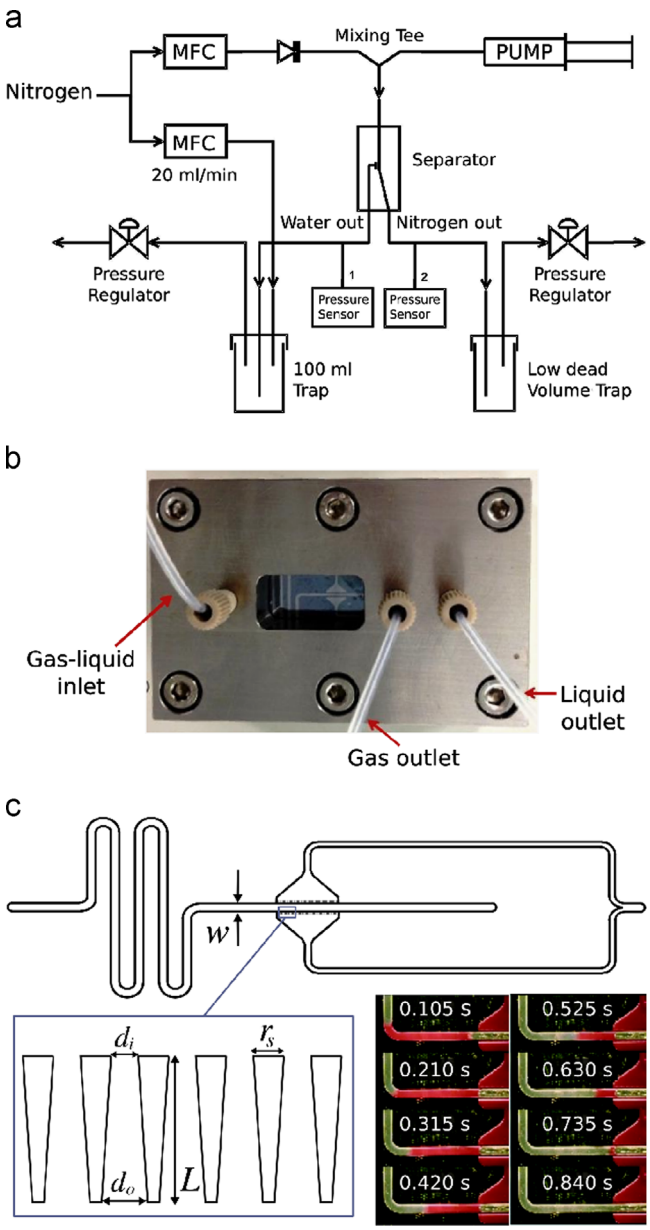

Fig. 1. (a) Process flow diagram of a capillary separator apparatus. (b) Image of the experimental device showing the separator with the location of the inlet and outlets. (c) Sketch of a typical separator. The left bottom panel shows a magnification of the microseparator area with details about the tapered capillaries. The right bottom panel shows snapshots of a typical gas–liquid separation experiment, where the liquid phase is depicted in red. (For interpretation of the references to colour in this figure legend, the reader is referred to the web version of this paper.)

470 mJ/cm^2, approximately equivalent to exposure of 300 nm UV light for 35 s. The photoresist was then aged for 30 min at room conditions to reinforce its adhesion on the silicon surface. The patterns were developed by immersing the wafers into a standard photoresist developer (Shipley Microposit MF-26A), for 80 s. After thorough rinsing, a final post-baking process at 110 °C for 90 s was carried out.

The patterned wafers were etched by deep reactive ion etching (STS ASE). All wafers, apart from the one corresponding to the GLS separator, were subjected to oxygen plasma treatment (Tepla). The etched height of the micro-channels was measured by a surface profiler (Veeco Dektak 8). The wafers were cut into the designed dimension using an automated precision dicing saw (Disco DADS 3230). The etched chip was anodically bonded with a glass (Corning 7740) plate with predrilled connection ports. The silicon and glass chips were cleaned with Piranha solution at 100 °C for 15 min to ensure that there was no contaminant attached on the bonding surfaces. They were rinsed with deionized water and dried thoroughly by blowing nitrogen.

Table 1
Specification of the separators used in this study. Spatial dimensions correspond to width × height. Widths were measured from microscopic pictures (Figs. 2 and 3) and heights were measured by surface profiles. All units are in μm. N and r_s are the total number of capillaries (including both sides of the main channel) and capillary spacing, respectively. The standard deviations for the capillary dimensions d_i, d_o, and r_s are consistently smaller than 0.2 μm in all separators. The values of d_{eff} and h_{eff} correspond to sides of an effective constant cross-sectional area of a channel obtained with COMSOL simulations (see Appendix A).

Separator	Main channel ($w \times h$)	N	r_s	Capillary inlet ($d_i \times h$)	Capillary outlet ($d_o \times h$)	Cross-section ($d_{eff} \times h_{eff}$)
GLS	600 × 300	70	92.9	47.1 × 300	24.7 × 300	31.1 × 300
P1	600 × 119	276	18.8	11.2 × 119	25.9 × 119	15.3 × 119
P2	600 × 109	300	45	5 × 109	25.6 × 109	10.1 × 109
P3	600 × 118	160	42.7	7.3 × 118	25.6 × 118	12.8 × 118
P4	600 × 125	160	42.9	7.1 × 125	6.5 × 125	

3.2. Experimental procedure

Initially nitrogen (>2 barg) was fed to two mass flow controllers (Bronkhorst 0–1 ml/min and Brooks 0–500 ml/min), the first was passed through a non-return valve and a pressure indicator to a mixing tee (Upchurch, PEEK, 1 mm ID). Into this tee was also fed the liquid stream via a syringe pump (PHD ULTRA, Harvard Apparatus) (see Fig. 1a). The resultant gas–liquid stream was then fed to the inlet of the separator. The gas outlet of the separator was passed through a low-dead-volume trap (Glass vial volume ca. 2 ml) via a pressure indicator to a manual pressure regulator (Swagelok Compact Piston-Sensing Back-Pressure Regulator KCB Series, 0–50 psi). The liquid stream was then fed via a pressure indicator into a 100 ml liquid trap that also had a stream of nitrogen (20 ml/min) (fed from the second mass flow controller) entering to increase the mass flow through the subsequent manual pressure regulator. The pressure indicators (40PC series, Honeywell, 0–2 bar) were calibrated via a digital hand-held pressure gauge (C9555 pressure meter, Comark Ltd, 0–30 psi) and the mass flow controllers via a bubble meter. The nitrogen supply (~5 bar) was turned on and the two mass flow controllers were set at 0.35 ml/min (gas inlet) and 20 ml/min (make-up stream). The liquid and gas flows were started, and the two pressure regulators adjusted so that the gas outlet pressure indicator reads ~450 mbar and the liquid outlet pressure indicator ~430 mbar. After the system had equilibrated and the pressure indicators stabilised, the pressure difference was carefully adjusted via the liquid outlet pressure regulator. Due to the make-up gas flowing through the liquid exit, the liquid outlet pressure stabilised within a few seconds after adjustment while any change to the gas outlet pressure took up to 5 min to stabilise. See Fig. 1c for an example of a gas–liquid separation experiment.

The pressure difference was increased until gas breakthrough was observed using a microscope (VHX-600 Digital Microscope with VH-Z20R lens). The presence of small bubbles in the liquid collection ducts indicated the onset of gas-to-liquid breakthrough. To measure the liquid-to-gas breakthrough the pressure difference ($P_G - P_L$) was slowly reduced until liquid was observed in the gas outlet tubing. All pressure readings were accurate to ±5 mbar. Static gas-to-liquid breakthrough pressure differences were measured by stopping the liquid flow when the capillaries and liquid

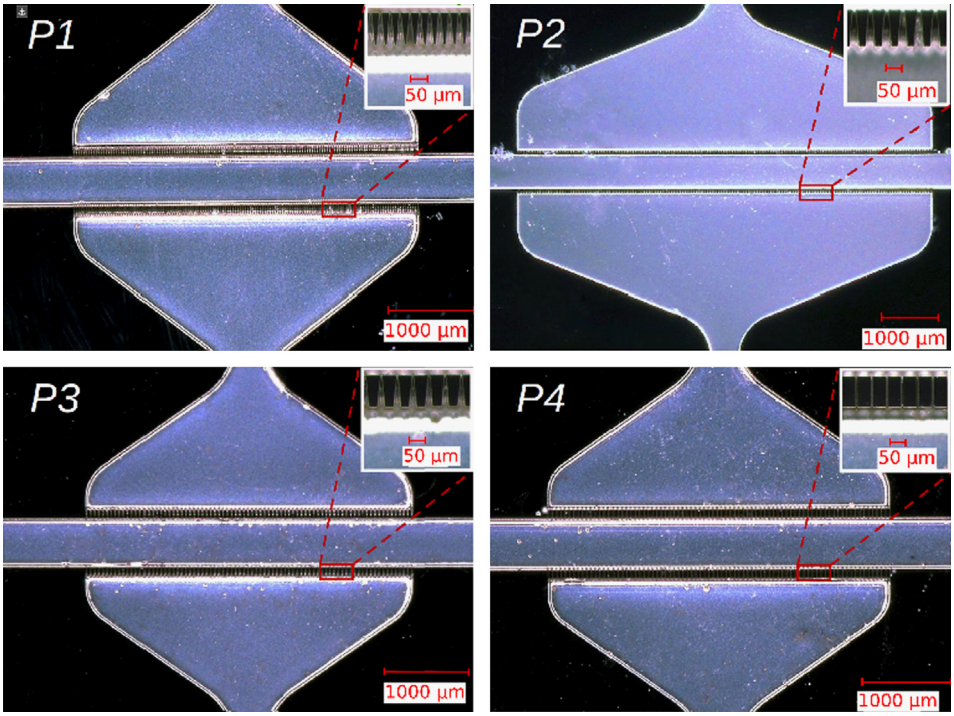

Fig. 2. Microscope images of the different P-series separators used in this work. The inset shows a magnification of the capillaries.

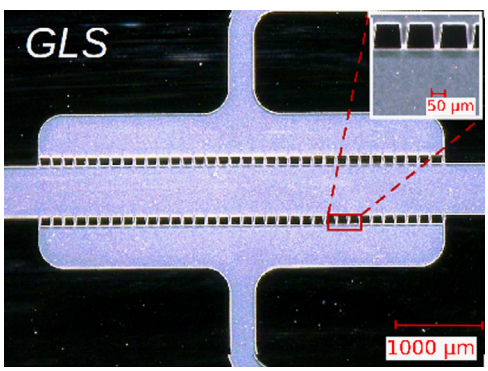

Fig. 3. Microscope image of the GLS separator. The inset shows a magnification of the capillaries.

collectors were free of gas and the pressure difference was increased until gas was seen to enter the capillaries.

4. Experimental results

Initial measurements were carried out using nitrogen and water as the gas and liquid streams, respectively. The gas flow rate (Q_G) was fixed at 0.35 ml/min and the liquid (Q_L) increased from 0.003 ml/min in logarithmic steps of 1×10^{-2} ml/min until no further complete separation was observed. Close to the breakthrough limit incremental linear steps were used. Each of the separator breakthrough pressures was measured three times and no variation was observed indicating that any experimental errors were within the measurement error.

4.1. Static gas-to-liquid breakthrough

We considered first the GLS separator in static conditions ($Q_L = 0$). In this situation the gas-to-liquid breakthrough pressure difference ($\Delta P_{G>L}$) was measured at 4500 Pa which is 71% of the theoretical value ($\Delta P_c = 6325$ Pa) given by Eq. (3), with $\gamma = 0.072$ N m^{-1}, and $d = d_o$ and h given in Table 1. One possible reason for such a discrepancy was thought to be the nature of the capillary channel surface. During fabrication the silicon is repeatedly cycled between an etching phase and a passivation phase. This passivation phase employs C_4F_4 which when deposited on the channel wall forms a Teflon-like layer, which if not completely removed will affect the contact angle of any liquid–gas interface and thus the capillary pressure. It is believed that the subsequent Piranha solution wash did not effectively remove this residue. The literature suggests that oxygen plasma treatment can remove the Teflon residues (see e.g. Lindroos et al., 2010). To this end, another separator from the same wafer was treated with several cycles of oxygen plasma (3 × 3 min) to clean the silicon surface. This wafer was bonded to glass and its measured static $\Delta P_{G>L}$ was found to be 8700 Pa which is significantly higher than the untreated GLS separator, and closer to the theoretical prediction. Given the success of the oxygen plasma treatment in maximising $\Delta P_{G>L}$, all the P-series separators were similarly treated. The results for the static $\Delta P_{G>L}$ are shown in Table 2, where we can observe reasonable agreement with the theoretical prediction ΔP_c. The higher experimental breakthrough values may be due

Table 2
Experimentally determined breakthrough conditions for the separators. Pressure difference and flow rate are given in Pa and ml/min, and $\overline{Q_L}$ and $\overline{\Delta P}$ are the corresponding values at $\Delta P_{G>L} = \Delta P_{L>G}$. GLS* corresponds to a O_2 plasma treated separator. The $\Delta P_{G>L}/\Delta P_c$ ranges are calculated to account for measurement error.

Separator	Liquid phase	$\Delta P_{G>L}$ static (Pa)	ΔP_c (Pa)	$\Delta P_{G>L}/\Delta P_c$ (%)	$\overline{Q_L}$ (ml/min)	$\overline{\Delta P}$ (Pa)
GLS	H_2O	4500 ± 500	6325	63–79	0.119	3800
GLS*	H_2O	8700 ± 500	6325	130–146	0.754	500
P1	H_2O	15,500 ± 500	14,050	106–114	0.189	11,000
P2	H_2O	30,000 ± 500	30,120	98–102	0.800	17,000
	EtOH	9400 ± 500	9200	97–108	0.075	7300
P3	H_2O	26,000 ± 500	21,020	121–126	0.189	16,000
	EtOH	9000 ± 500	6430	132–148	0.048	7300
P4	H_2O	24,500 ± 500	21,380	112–117	0.189	20,500

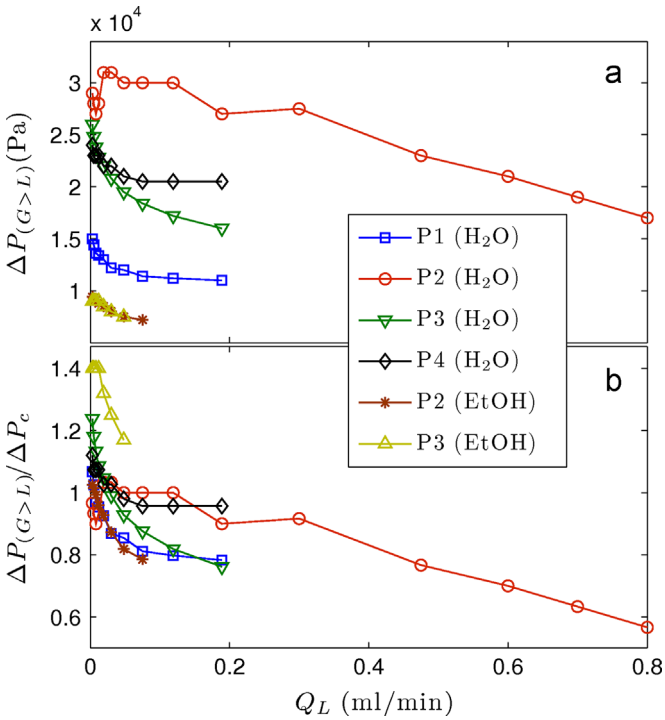

Fig. 4. (a) Experimental values of the gas-to-liquid breakthrough pressures for the different P-series separators plotted against the liquid flow rate. Panel (b) shows the same pressures as in (a) scaled by the corresponding capillary pressure ΔP_c.

to imperfect etching, resulting in a smaller size of the opening at the bottom of the capillary. This was confirmed after cutting the separators at the capillaries and looking at their cross-section.

4.2. Breakthrough under flow conditions

For liquid flow conditions ($Q_L > 0$), the experimental values of both gas-to-liquid $\Delta P_{G>L}$ and liquid-to-gas breakthrough pressure difference ($\Delta P_{L>G}$) as functions of Q_L were measured for the P-series separators. Water was the wetting phase for all the separators and additionally ethanol for the P2 and P3 separators. The results are presented in Figs. 4a and 5a. Attempts were made to separate ethanol and nitrogen using the GLS separator but this was unsuccessful. This could be due to the lower capillary pressure and instabilities in the setup e.g. pumps. We proceed now to analyse the different experimental results for either breakthrough case.

Flow gas-to-liquid breakthrough: Theoretically the only factors affecting the gas-to-liquid breakthrough pressure should be the gas–liquid surface tension and the dimensions of the smallest cross section in the capillary (which is the capillary inlet in Table 1 except for the GLS separator which is the capillary outlet). Note that all these factors are accounted for in the capillary pressure given by the Young–Laplace equation (3). Any possible correlation between the different separators could be hence identified by computing the ratio of the breakthrough pressure difference $\Delta P_{G>L}$ to the capillary pressure difference ΔP_c. Fig. 4b shows this quantity plotted versus the liquid flow rate, where we can observe that there is a reasonable correlation between the P-series separators.

Flow liquid-to-gas breakthrough: Fig. 5a shows the experimental values of $\Delta P_{L>G}$ against the liquid flow rate (Q_L). It is initially evident that there are two correlated groups, namely group 1: [P1 (H_2O) & P2 (H_2O) & P2 (EtOH) & P3 (EtOH)] and group 2: [P3 (H_2O) & P4 (H_2O)]. We note however that all separators show similar liquid-to-gas breakthrough behaviour at low liquid flow rates, and

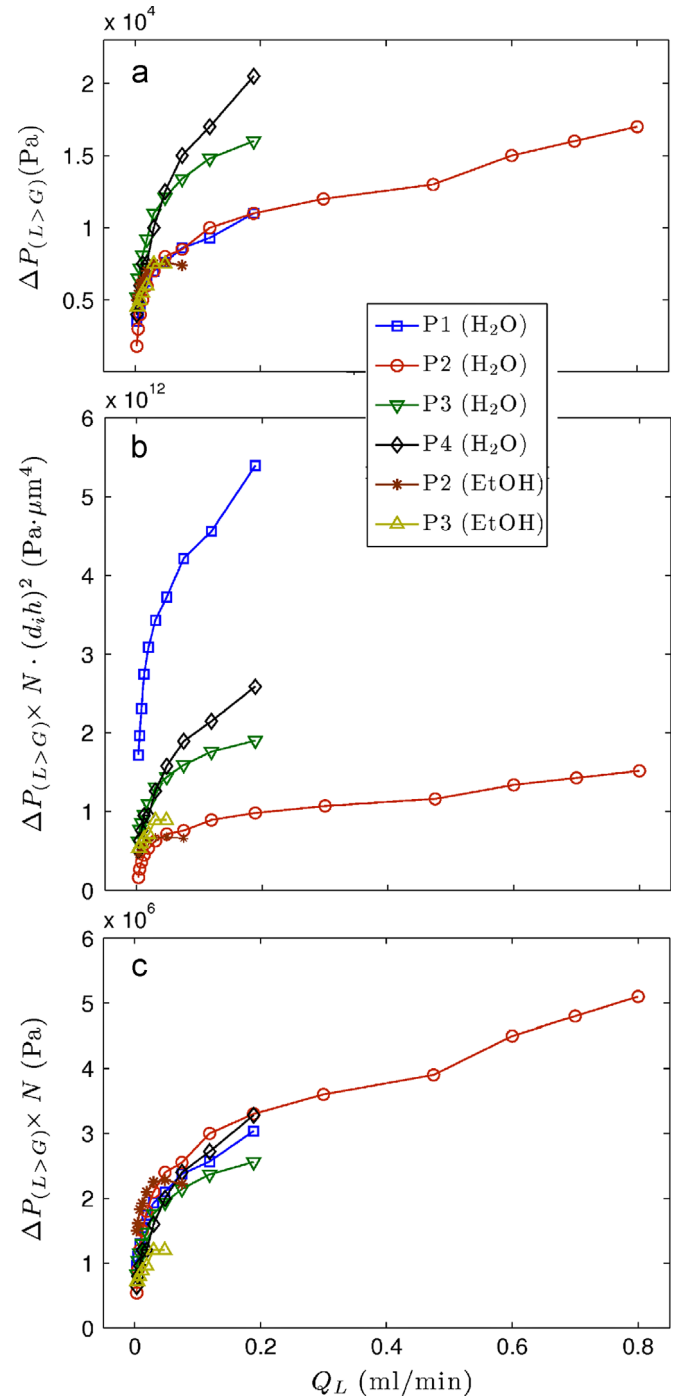

Fig. 5. (a) Experimental values of the liquid-to-gas breakthrough pressures for the different P-series separators plotted against the liquid flow rate. Panel (b) shows the same pressures multiplied by the product of the number of capillaries and the squared capillary area $A^2 = (d_i h)^2$. Panel (c) shows the same pressures multiplied by the number of capillaries only.

deviations become more pronounced at high flow rates. In Fig. 5b the breakthrough pressures are scaled by $1/(NA^2)$, that is according to Eq. (6). The curves do not show a good correlation indicating that the geometrical factors of Eq. (6) are not appropriate to describe the breakthrough pressures. Indeed, if we look at the features of the two groups of separators 1 and 2, we note that a distinct difference between them is the number of capillaries N. Hence, we next scale the breakthrough pressures by $1/N$ (Fig. 5c). It can be seen that all P-series datasets exhibit now a good correlation with each other, indicating that the number of

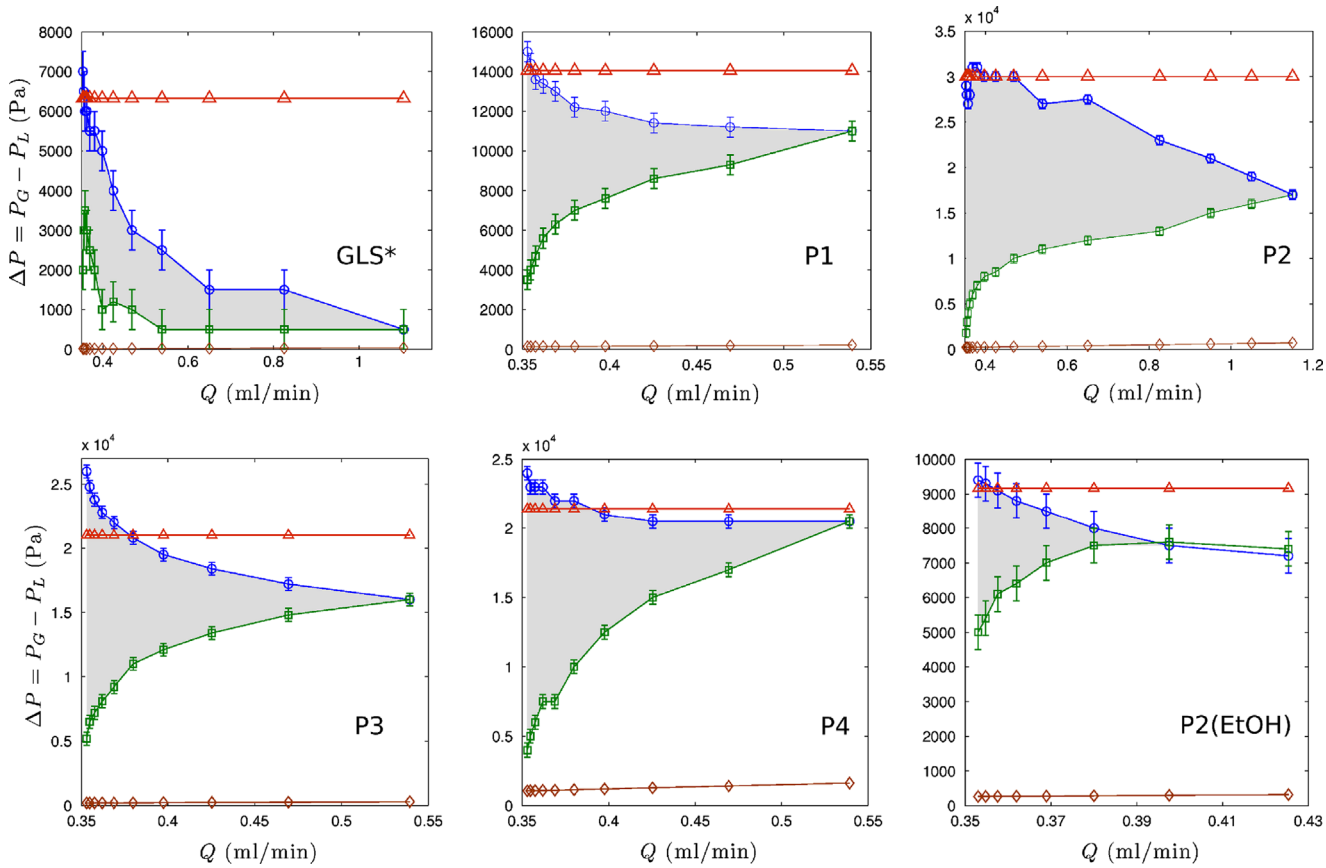

Fig. 6. Stable operating ranges (grey areas) of the different separators. $Q = Q_G + Q_L$ represents the total flow rate. Circles (○) and squares (□) correspond to the gas-to-liquid and liquid-to-gas breakthrough pressures, respectively. Triangles (△) and diamonds (◇) correspond to the theoretical values of Eqs. (3) and (6), respectively.

capillaries, but not the capillary geometry, plays an important role. It is important to emphasise that this is in agreement with the equation derived in Section 5 (see Eq. (16)) which suggests that the nonlinear behaviour of the breakthrough pressure as a function of Q is independent of the capillary geometry and depends on the number of capillaries via the parameter β_N (see Section 5.1 for details).

Operating range diagrams: We present here all the experimental data for both gas-to-liquid and liquid-to-gas breakthrough pressures plotted against the total flow rate ($Q = Q_G + Q_L$) in the same figure so we can define the operating ranges as the area between both curves (see grey area in Fig. 6). The experimental data is also compared to the theoretical prediction of Eqs. (3) and (6) which correspond to the gas-to-liquid breakthrough pressure difference ($\Delta P_{G>L}$) and liquid-to-gas breakthrough pressure difference ($\Delta P_{L>G}$), respectively.

The theoretical results for liquid-to-gas breakthrough were obtained by means of computations of the commercial CFD software COMSOL (see Appendix A). We first note that at low flow rates ($Q < 0.4$ ml/min) the gas-to-liquid breakthrough pressure difference exhibits a nearly constant behaviour which is in reasonable agreement with the theoretical prediction of Eq. (3), especially for the P1, P2 and P4 separators. For slightly higher flow rates ($0.4 < Q < 0.55$ ml/min) the experimental results exhibit high deviations from the theoretical values which become higher for $Q > 0.55$ ml/min (see experiments for separator P2 with water) indicating that at this range of flow rates other effects occurring at the entrance of the capillaries may need to be taken into account.

On the other hand, we also note that the linear behaviour for the liquid-to-gas breakthrough which is predicted in Eq. (6) is not observed. It is worth mentioning though that the stable operating ranges as depicted in Fig. 6 decrease with the flow rate, something that has also been reported in liquid–liquid separators (see Castell et al., 2009, Fig. 5). To understand better the experimental results we develop in the next section a theoretical approach that takes into account additional factors such as the pressure drop along the liquid slug.

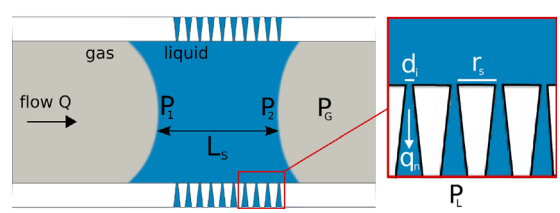

Fig. 7. Liquid slug advancing into a two-dimensional microchannel. Computations were done with the CFD software TransAT.

5. Theoretical framework and computations

5.1. Liquid-to-gas breakthrough theory

Following the experimental setup described in Section 3, we consider a liquid–gas slug advancing through a microseparator which is compound of N tapered capillaries placed on each side of the main channel and separated apart by a distance r_s (see Fig. 7). In this situation the speed of the slug is approximately $(Q_L + Q_G)/A_m$, where $A_m = hw$ is the area of the main channel.

Assuming that the slug is covering all capillaries, the critical state for which the liquid slug does not advance through the main channel and is being imbibed by the capillaries is achieved whenever the sum of all the capillary flow rates is balanced by the main channel inlet flow rate, which we assume to be given by the total flow rate $Q = Q_L + Q_G$. If we denote the flow rate at each capillary as q_n, the condition is mathematically described as

$$Q = 2\sum_{n=1}^{N/2} q_n. \tag{7}$$

In contrast to assuming that q_n is the same for all the capillaries as we did in Section 2 we consider now that the flow rate q_n actually depends on the position of the capillary along the main channel, so that for each capillary we have the Hagen–Poiseuille law applied locally

$$q_n = \alpha_c \frac{\Delta P_n}{\eta L}, \tag{8}$$

where we have defined α_c to be a generic geometrical factor, and $\Delta P_n = P_n - P_L$ is the pressure drop along the capillary, where P_n is the pressure right at the entrance of the capillary n, i.e. at the beginning of the capillary and in the middle of d_i, and P_L its exit pressure, which is controlled externally (note that we are assuming negligible pressure drop up to the measurement point). P_n is not known *a priori* and needs to be estimated. To this end we are going to consider that the pressure field inside the liquid slug is given by the Laplace equation, $\partial_x^2 P(x) = 0$. This means that we are essentially assuming most of the flow along the vertical (cross-stream) direction y of the main channel occurs right at the entrance of the capillaries so we can approximate the pressure inside the slug to be independent of y (this can also be justified within a slow-slug motion approximation). By imposing the following boundary conditions at the gas–liquid and liquid–gas interfaces of the slug: $P(0) = P_1$ and $P(L_S) = P_2$ (see Fig. 7) we obtain the following expression:

$$P(x) = P_1 - \frac{P_1 - P_2}{L_S} x, \tag{9}$$

where L_S is the length of the liquid slug. The pressure P_n at the entrance of each capillary can finally be obtained by rewriting the above expression in a discrete form. In particular, we take that $x_n = n\Delta x$ for $n = 1, \ldots, N/2$ so we get

$$P_n = P_1 - n\frac{P_1 - P_2}{L_S}\Delta x, \tag{10}$$

where $\Delta x = d_i + r_s$ is the sum of the capillary inlet width d_i and the capillary separation r_s.

By inserting Eq. (10) into (7) via (8) we obtain the following relation:

$$\frac{\eta L}{\alpha_c N} Q = P_1(1 - \beta_N) + P_2 \beta_N - P_L, \tag{11}$$

where $\beta_N = \Delta x(N/2 + 1)/(2L_S)$. It is important to remark here a few points. First, we are considering the limit case where the liquid slug is sufficiently large so it covers all capillaries. In this situation, and for a given flow rate, the achievement of the separation process can be considered independent of the initial slug length as long as Eq. (7) is satisfied (note that only the duration of the separation process will depend on the slug length). We therefore take a generic slug length which is equal to the length of the microseparator, i.e. $L_S = \Delta x N/2$, giving rise to $\beta_N = (N+2)/(2N)$. Second, and based on the experimental observations of Fig. 1c and the CFD computations presented in the next section (see Fig. 10b), we assume that during the critical separation process (which gives the liquid-to-gas breakthrough pressure) the advancing liquid/gas interface remains stationary while the receding gas/ interface advances at a speed dictated by the flow rate.

Based on these considerations, we proceed to the next and final step to determine the pressure difference across the gas–liquid and liquid–gas interfaces of the liquid slug, i.e. $\Delta P_1 = P_{in} - P_1$ and $\Delta P_2 = P_G - P_2$, respectively, where P_{in} is the gas pressure at the inlet of the main channel and P_G at the outlet, which is controlled externally. As stated above, we consider the advancing liquid/gas interface to be stationary and hence ΔP_2 can be considered to be constant and equal to the equilibrium capillary pressure difference of the main channel, which we denote as P_c^{m} and is given by the Young–Laplace equation (3) applied to the main channel, i.e.:

$$P_c^{\mathrm{m}} = 2\gamma \cos(\theta_{eq})\left(\frac{1}{h} + \frac{1}{w}\right) \tag{12}$$

so that we have $\Delta P_2 = P_c^{\mathrm{m}}$, where θ_{eq} is the equilibrium contact angle and w and h are the transversal width and height of the main channel, respectively (see Table 1). On the other hand, we shall assume that the apparent contact angle θ_1 at the gas–liquid interface of the main channel is affected by the flow rate, and is given by the relation (Bonn et al., 2009; Kreutzer et al., 2005)

$$(\pi - \theta_1)^3 = (\pi - \theta_{eq})^3 + \lambda Ca, \tag{13}$$

where λ is a constant that depends on the microscopic properties at the contact point level, and $Ca = \eta U/\gamma$ is the capillary number with $U = Q/A_m$ being a typical velocity. By taking then that the pressure difference across interface 1 will be given by the Young–Laplace relation $\Delta P_1 = P_{in} - P_1 = 2\gamma \cos(\theta_1)(1/h + 1/w)$, and assuming small contact angles so that $\cos(\theta_1) \simeq 1 - \theta_1^2/2$, we obtain

$$P_1 = P_{in} - \frac{P_c^{\mathrm{m}}}{\cos\theta_{eq}} + \frac{P_c^{\mathrm{m}}}{2\cos\theta_{eq}}[\pi - ((\pi - \theta_{eq})^3 + \lambda Ca)^{1/3}]^2. \tag{14}$$

By substituting the expressions for P_1 and P_2 into Eq. (11) we finally obtain

$$\Delta P_{L>G} = P_c^{\mathrm{m}} \Lambda_N + (P_G - P_{in})(1 - \beta_N) + \frac{\eta L}{\alpha_c N} Q - \frac{1 - \beta_N}{2\cos\theta_{eq}} P_c^{\mathrm{m}} [\pi - ((\pi - \theta_{eq})^3 + \lambda Ca)^{1/3}]^2, \tag{15}$$

where $\Lambda_N = \beta_N + (1 - \beta_N)/\cos\theta_{eq}$. The above expression contains unknown parameters which need to be fitted from experimental data. In particular, we will rewrite it as

$$\Delta P_{L>G} = -\frac{1 - \beta_N}{2\cos\theta_{eq}} P_c^{\mathrm{m}} [\pi - ((\pi - \theta_{eq})^3 + a_3 Q)^{1/3}]^2 + P_c^{\mathrm{m}} \Lambda_N + a_1 + a_2 \frac{\eta L}{N \alpha_c} Q, \tag{16}$$

where a_1 has to be of similar order to $P_c^{\mathrm{m}} \sim 1.4 \times 10^3$ Pa, a_2 is the geometrical correction due to tapered channels and deviations from the Hagen–Poiseuille law, and $a_3 = \lambda\eta/(hw\gamma)$ contains information about the microscopic details of the contact line.

The numerical results of the experimental data fits are presented in Fig. 8. We have considered here an equilibrium contact angle of $\theta_{eq} = 20^\circ$ as we are assuming small contact angles (other values, namely 5° and 10°, have also been considered observing no quantitative difference in the results). We observe that the experimental data can be described by Eq. (16). The numerical values of the data fits are presented in Table 3 and they have the expected orders of magnitude. Although the above analysis does not provide closure and leaves three parameters, $a_{1,2,3}$, to be determined experimentally, it does provide the exponent 2/3 for the Q dependence of $\Delta P_{L>G}$ in Eq. (16) which is crucial for the good agreement with the data in Fig. 8.

5.2. Computations

Following the experimental designs for the separators, we perform a CFD-type computational modelling with a similar structure to that in the separator P2 which consists of tapered capillaries of $L=100$ μm length and an inlet and an outlet width of $d_i=5$ and $d_o=25$ μm, respectively. We use the commercial CFD code TransAT (Transport phenomena Analysis Tool, http://www.ascomp.ch/transat.html), developed at ASCOMP, a multi-physics, finite-volume code based on solving multi-fluid Navier–Stokes equations. The code uses multi-block structured meshes, along with MPI based parallel capabilities. The system is nondimensionalised by using the microchannel width ($w=600$ μm) as a length scale, a nominal velocity of $U=10^{-1}$ m/s, and the time scale of $T=L/U$. We impose a constant gas flow rate in a two-dimensional (2D) system of a liquid/gas slug (see Fig. 9).

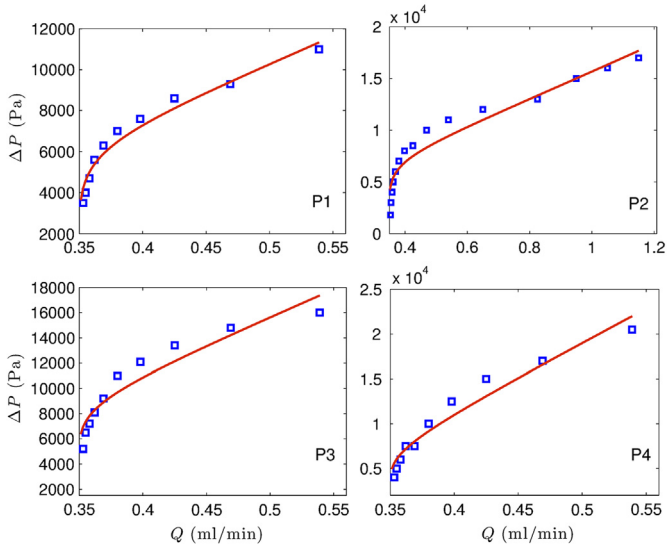

Fig. 8. Experimental values of the liquid-to-gas breakthrough pressure for water (squares) with a data fit curve (red solid line). (For interpretation of the references to colour in this figure legend, the reader is referred to the web version of this paper.)

Table 3
Numerical values from the experimental data fits.

Separator	$a_1(\times 10^3)$	a_2	$a_3(\times 10^4)$
P1	3.3	37.4	68.7
P2	4.2	7.8	32.3
P3	5.9	25.4	62.5
P4	4.5	17.3	62.4

In this situation, we initially place a liquid slug covering all the capillaries (see left panels of Fig. 9) and fix a zero gas flow rate and zero pressure gauge at the capillaries outlet (i.e. $P_L=0$) until the equilibrium state is reached. By doing this, we make sure that the initial state before turning on the gas flow rate is that dictated by the corresponding equilibrium contact angle (which we have considered to be either $\theta_{eq}=20^\circ$ or 45°, observing that the results did not change for this range of small angles). Once the equilibrium state has been reached we turn the gas flow rate on and change the pressure P_L at the capillaries outlet until we observe that the liquid slug does not advance, indicating hence that condition (Eq. (7)) is achieved and we have reached the breakthrough critical pressure difference $\Delta P_{L>G}$ (see middle panels in Fig. 9). Note that for pressure differences below $\Delta P_{L>G}$ the total sum of the flow rates of the capillaries cannot balance the imposed gas flow rate of the main channel and as a consequence the liquid slug advances through the main channel (top panels in Fig. 9). On the other hand, for pressure differences higher than $\Delta P_{L>G}$, the total flow rate coming out from the capillaries is higher than the gas flow rate so the liquid can be completely absorbed by the capillaries achieving an optimal condition for the separator (see bottom panels in Fig. 9).

The breakthrough pressure differences for different flow rates are presented in Fig. 10 where we observe a linear behaviour at relatively low flow rates. It should be noted that for gas flow rates higher than 0.17 (in non-dimensional units) the gas–liquid interface on the left-hand-side of the slug starts to exhibit fingering leaving a thin-film of liquid behind (see Fig. 11). At this point, the slug starts to break into small droplets and the separation process is not efficient anymore. The reason why we do not observe the

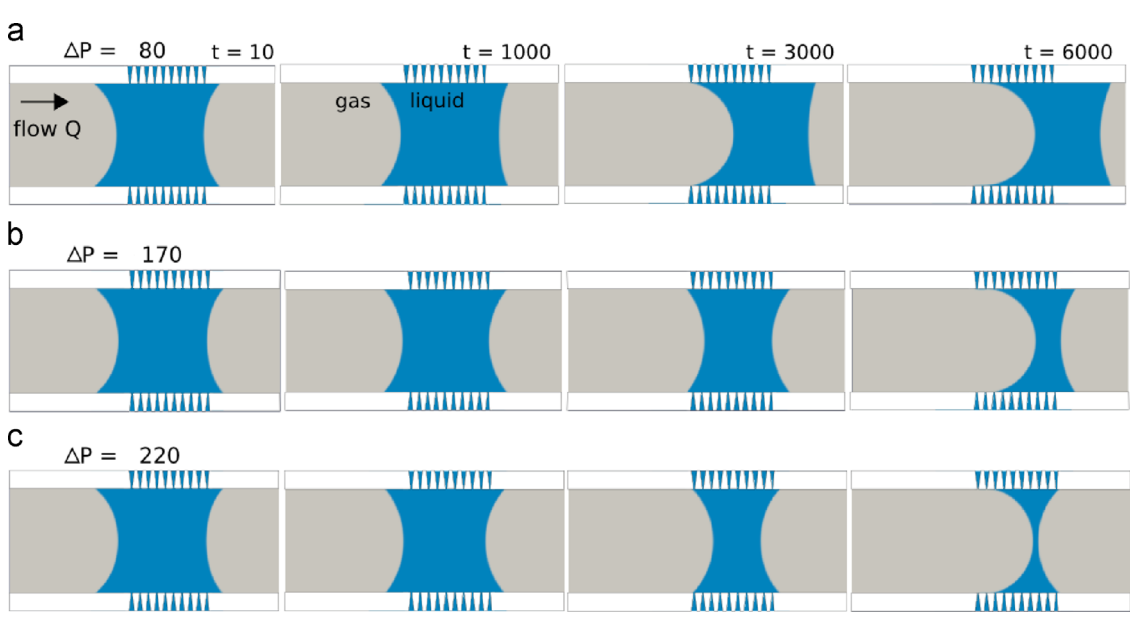

Fig. 9. 2D numerical computations of the separator P2 by imposing a constant gas flow rate at the inlet of the main channel. Top panels show an example of a pressure difference $\Delta P=P_G-P_L$ being below the critical breakthrough pressure difference. Panels in the middle correspond exactly to the breakthrough pressure, and the bottom panels above it. Computations were done with TransAT and the numerical values are given in dimensionless units.

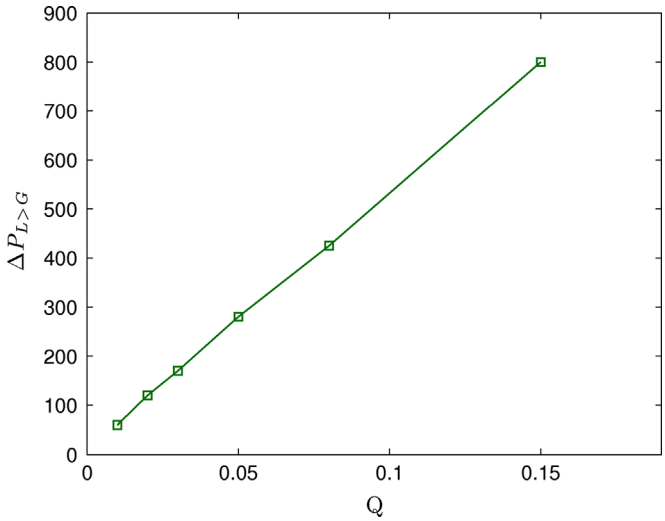

Fig. 10. 2D numerical results of the breakthrough pressure as a function of the imposed constant total flow rate Q of the separator P2. Computations were done with TransAT and the values are given in dimensionless units.

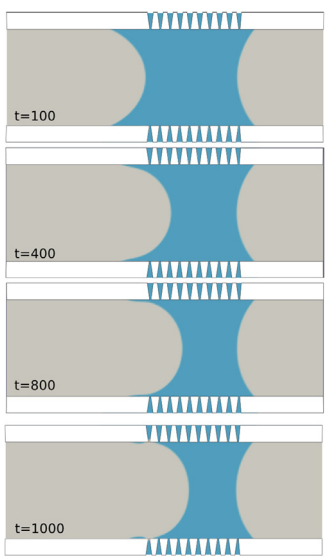

Fig. 11. Example of computations of high gas flow rate. As shown in the bottom panels, the gas–liquid interface leaves a thin film and starts to develop a finger until it breaks into small droplets.

experimental nonlinear behaviour of $\Delta P_{L>G}$ as a function of Q in the computations can be attributed to a nontrivial interaction between the imposed gas and the liquid flow rate at the entrance of the experimental main channel which in turn prevents the slug developing fingering phenomena. Note however that fingering phenomena and in particular the formation of thin films are quite difficult to observe experimentally and the precise effect of residual liquid on multiphase flows in microchannels is something not well-known (see e.g. Cheah et al., 2013). Also, note that three-dimensional effects, such as corner flows, which could be relevant in the experiments, especially at high flow rates, are not taken into account in the 2D simulations.

6. Conclusions

We have presented a combined experimental–theoretical study of gas–liquid capillary separation in microsystems comprising a main channel with a series of capillaries which are attached to either side of it. Due to the capillary pressure the multiphase flow passing through the main channel can be separated so that the liquid is absorbed by the small capillaries while the gas phase is collected at the outlet of the main channel. We have considered capillaries with either constant or tapered cross-sectional area. Gas-to-liquid breakthrough under static conditions is in reasonable agreement with the predictions of the Young–Laplace equation.

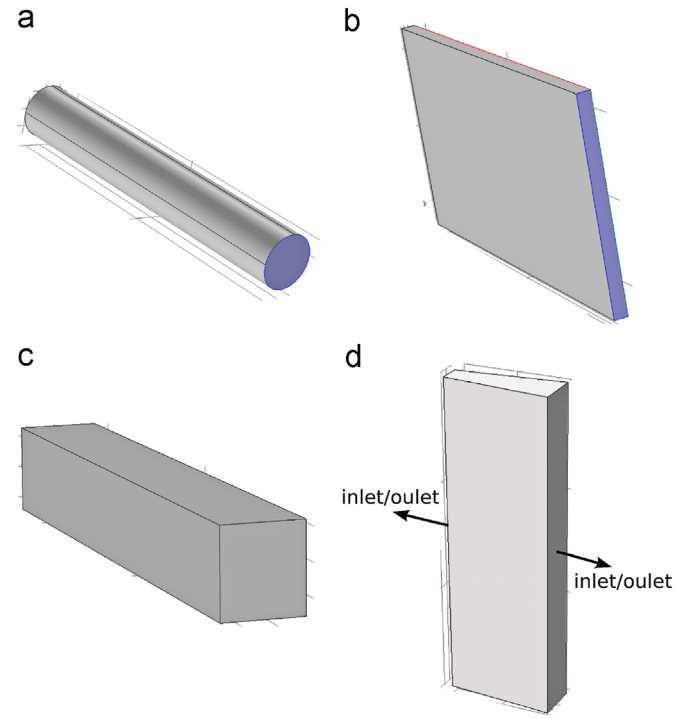

Fig. 12. Different capillary geometries used with COMSOL software to calculate the corresponding pressure drop.

Under continuous flow conditions our experimental results have revealed that the gas-to-liquid breakthrough pressures are in qualitative agreement with the theoretical capillary pressures at relatively low flow rates, showing some deviations at higher flow rates. On the other hand, we have observed that the liquid-to-gas breakthrough pressures exhibit a nonlinear relation with the imposed liquid flow rate at the inlet of the system. This behaviour cannot be captured by a simple Hagen–Poiseuille law description. To this end we have developed a theoretical approach that takes into account the effects of the flow on the interface curvature of the liquid–gas slug, which we have been able to fit with the experimental data. The derivation of this equation has been partly based on observations from CFD simulations of microseparators that showed that the advancing liquid/gas interface of the slug is not affected by the flow rate at the breakthrough pressure. In addition, we have observed from CFD simulations that at high inlet flow rates several non-trivial phenomena start to be important, and in particular our numerical results have shown the emergence of fingering and interface breaking.

Therefore, the operating ranges of the microseparator (i.e. breakthrough pressures) strongly depend on the inlet flow conditions of the system, something that needs to be taken into account in the design and operation of such units. There are of course several open questions, i.e. how the particular geometry of the capillaries (Amador et al., 2003; Yatsyshin et al., 2013) and the presence of additional complexities associated with wetting (i.e. hydrophobic conditions, Queralt-Martín et al., 2011 or chemical/topographical heterogeneities, Savva et al., 2010; Wylock et al.,

2012; Vellingiri et al., 2011; Schmuck et al., 2012) affect liquid–gas flows in microfluidic devices. We shall address these and related issues in future studies.

Nomenclature

A	area of the capillary (μm^2)
A_m	area of the channel (μm^2)
C	compactness factor
Ca	capillary number
d_0	capillary outlet width (μm)
d_i	capillary inlet width (μm)
d_{eff}, w_{eff}	sides of effective channel (μm)
h	height of the main channel (μm)
L	length of the capillary (μm)
L_S	liquid slug length (μm)
N	total number of capillaries
P_G	pressure at the gas outlet (Pa)
P_L	pressure at the liquid outlet (Pa)
ΔP	gas–liquid pressure difference (Pa)
P_c^m	channel Young–Laplace ΔP (Pa)
ΔP_c	capillary Young–Laplace ΔP (Pa)
$\Delta P_{G>L}$	gas-to-liquid breakthrough ΔP (Pa)
$\Delta P_{L>G}$	liquid-to-gas breakthrough ΔP (Pa)
P_{in}	gas pressure at inlet (Pa)
P_n	pressure at capillary entrance (Pa)
P_r	channel perimeter (μm)
Q	total flow rate (ml/min)
Q_G	gas flow rate (ml/min)
Q_L	liquid flow rate (ml/min)
q	capillary local flow rate (ml/min)
R_1, R_2	radii of interface curvature (μm)
r_s	separation between capillaries (μm)
U	typical velocity (μm/s)
w	width of the main channel (μm)
Greek symbols	
α, α_c	geometric factors
γ	gas–liquid surface tension (mN/m)
η	liquid viscosity (Pa s)
θ	contact angle (deg)
θ_{eq}	equilibrium contact angle (deg)
κ	interface curvature (μm)
λ	microscopic interactions

Acknowledgements

We thank the anonymous referees for useful comments and suggestions. We are grateful to ASCOMP for hospitality and for useful discussions on the use of TransAT. We acknowledge partial financial support from the European Framework 7 via Grant no. 214919 (Multiflow), the European Research Council via Advanced Grant no. 247031, UCL and Imperial College through the "Kick-Start" initiative, and the EPSRC.

Appendix A. Computations of the Hagen–Poiseuille flow

The numerical results presented in Fig. 6 that correspond to the Hagen–Poiseuille equation (6) for the tapered capillaries (as well as the data in Table 1) can be easily obtained by means of COMSOL computations as follows. We first considered simple geometries like those depicted in Fig. 12(a–c) and computed numerically the pressure drop. In all cases we found very good agreement with the theoretical prediction of Eq. (6) and the corresponding numerical values. Next, we constructed tapered geometries as the one shown in Fig. 12d and computed numerically the pressure drop versus the flow rate. The obtained data was used in conjunction with Eq. (6) to determine the appropriate equivalent constant cross-sectional channel to use when calculating the pressure drop in Fig. 6 (see the values of these effective cross-sectional areas in Table 1). We used the values of $\eta = 0.001$ Pa s and $\eta = 0.0012$ Pa s for the viscosity of water and ethanol, respectively.

References

Adamo, A., Heider, P.L., Weeranoppanant, N., Jensen, K.F., 2013. Ind. Eng. Chem. Res. 52, 10802–10808.
Amador, C., Angeli, P., Gavriilidis, A., Shaw, J., Wenn, D., 2003. In: Proceedings of the 2003 Fall AIChE Symposium (in CD-ROM).
Bahrami, M., Yovanovich, M.M., Culham, J.R., 2007. Int. J. Heat Mass Transf. 50, 2492–2502.
Bannock, J.H., Phillips, T.W., Nightingale, A.M., deMello, J.C., 2013. Anal. Methods 5, 4991–4998.
Bonn, D., Eggers, J., Indekeu, J., Meunier, J., Rolley, E., 2009. Rev. Mod. Phys. 81, 739–805.
Bruus, H., 2008. Theoretical Microfluidics. Oxford University Press, New York.
Butt, H.-J., Graf, K., Kappl, M. (Eds.), 2013. Physics and Chemistry of Interfaces. Wiley-VCH Verlag, Weinhem.
Castell, O.K., Allender, C.J., Barrow, D.A., 2009. Lab Chip 9, 338–396.
Cheah, M.J., Kevrekidis, I.G., Benziger, J.B., 2013. Langmuir 29, 9918–9934.
Gaakeer, W.A., de Croon, M.H.J.M., Van der Schaaf, J., Schouten, J.C., 2012. Chem. Eng. Sci. 207–208, 440–444.
Geschke, O., Klank, H., Telleman, P. (Eds.), 2004. Microsystem Engineering of Lab-on-a-Chip Devices. John Wiley & Sons, New York.
Günther, A., Jhunjhunwala, M., Thalmann, M., Schmidt, M.A., Jensen, K.F., 2005. Langmuir 21, 1547–1555.
Hartman, R.L., Sahoo, H.R., Yen, B.C., Jensen, K.F., 2009. Lab Chip 9, 1843–1849.
Hessel, V., Hardt, S., Lowe, H., 2005. Chemical Micro Process Engineering: Fundamentals, Modelling and Reactions. John Wiley & Sons, New York.
Hsieh, C., Alyousef, Y., Yao, S., 2006. In: Proceedings of ICNMM2006 Fourth International Conference on Nanochannels, Microchannels and Minichannels.
Krajl, J.G., Sahoo, H.R., Jensen, K.F., 2007. Lab Chip 7, 256–263.
Kraus, M., Krewer, U., 2011. Sep. Purif. Technol. 81, 347–356.
Kreutzer, M.T., Kapteijn, F., Moulijn, J.A., Kleijn, C.R., Heiszwolf, J.J., 2005. AIChE J. 51, 2428–2440.
Lindroos, V., Tilli, M., Lehto, A., Motooka, T. (Eds.), 2010. Handbook of Silicon Based MEMS Materials and Technologies. Elsevier, Oxford.
Mortensen, N.A., Okkels, F., Bruus, H., 2005. Phys. Rev. E 71, 057301.
Queralt-Martín, M., Pradas, M., Rodríguez-Trujillo, R., Arundell, M., Corvera-Poiré, E., Hernández-Machado, A., 2011. Phys. Rev. Lett. 23, 194501.
Sahoo, H.R., Kralj, J.G., Jensen, K.F., 2007. Angew. Chem. Int. Ed. 46, 5704–5708.
Savva, N., Kalliadasis, S., Pavliotis, G.A., 2010. Phys. Rev. Lett. 104, 084501.
Schmuck, M., Pradas, M., Pavliotis, G.A., Kalliadasis, S., 2012. Proc. R. Soc. A 468, 3705–3724.
Squires, T.M., Quake, S.R., 2005. Rev. Mod. Phys. 77, 977–1026.
TeGrotenhuis, W.E., Stenkamp, V., 2001. NASA/CR 2001-210955.
Vellingiri, R., Savva, N., Kalliadasis, S., 2011. Phys. Rev. E 84, 036305.
Whitesides, G.M., 2006. Nature 442, 368–373.
Wylock, C., Pradas, M., Haut, B., Colinet, P., Kalliadasis, S., 2012. Phys. Fluids 24, 032108.
Yatsyshin, P., Savva, N., Kalliadasis, S., 2013. Phys. Rev. E 87, 020402(R).